



# Structural and electrical properties of $\text{Bi}(\text{Mg}_{0.5}\text{Ti}_{0.5})\text{O}_3$ ceramic

Varsa Purohit<sup>1</sup> · Rajib Padhee<sup>2</sup> · R. N. P. Choudhary<sup>1</sup>

Received: 10 November 2017 / Accepted: 26 December 2017 / Published online: 3 January 2018  
© Springer Science+Business Media, LLC, part of Springer Nature 2018

## Abstract

Bismuth magnesium titanate  $\text{Bi}(\text{Mg}_{0.5}\text{Ti}_{0.5})\text{O}_3$  ceramic, fabricated by ceramic processing technique, has been characterized using various experimental techniques. Analysis of basic crystal structure using X-ray diffraction data has exhibited the orthorhombic system as a major phase. Microstructural analysis provided the quality of the sample. Detailed studies of electrical properties (dielectric constant, tangent loss, electrical modulus, conductivity and impedance) of  $\text{Bi}(\text{Mg}_{0.5}\text{Ti}_{0.5})\text{O}_3$  in a wide range of frequency (1 kHz–1 MHz) and temperature (25–480 °C) have provided various interesting results on antiferroelectric characteristics, conduction mechanism, structure–properties relationship, etc. An important role of interface in getting high dielectric material has been realized. The space charge polarization and Maxwell–Wagner dielectric relaxation in the material, particularly at low frequencies and high temperatures. Nyquist plots discuss the temperature-dependent contributions of grain effect. The frequency of the applied electric field and temperature strongly affect the electrical (AC) conductivity and transport properties of the material studied, and exhibiting semiconductor characteristics.

## 1 Introduction

Based on the value of dielectric parameters (dielectric constant as well as a dielectric loss), the devices are designed and fabricated. Study of these parameters with varying temperature and frequencies is one of the most convenient and responsive methods to study polycrystalline or ceramic materials. Ceramics with stable dielectric properties above 200 °C are useful to develop high-temperature capacitors for electronic applications [1, 2]. Some dielectric materials with high dielectric permittivity ( $\epsilon_r$ ) and small dissipation factor over a wide range of temperature and frequency are also useful for some electronic devices. As lead is a highly toxic, it has not been found suitable for many commercial applications and materials [3]. In order to get eco-friendly lead-free high dielectric constant materials for devices, attempts have been made to study a large number of solid solutions, complex or composites including;  $\text{BiScO}_3\text{--BaTiO}_3\text{--K}_{0.5}\text{Bi}_{0.5}\text{TiO}_3$  [1];  $\text{Na}_{0.5}\text{Bi}_{0.5}\text{TiO}_3\text{--}0.06\text{BaTiO}_3\text{--K}_{0.5}\text{Na}_{0.5}\text{NbO}_3$  [2];

$\text{BaTiO}_3\text{--Ba}(\text{Zn}_{0.5}\text{Ti}_{0.5})\text{O}_3$  [4];  $\text{BaTiO}_3\text{--Ba}(\text{Zn}_{0.5}\text{Ti}_{0.5})\text{O}_3\text{--BiScO}_3$  [5];  $\text{Na}_{0.5}\text{K}_{0.5}\text{NbO}_3\text{--LiTaO}_3\text{--BiScO}_3$  [6, 7];  $\text{Na}_{0.5}\text{Bi}_{0.5}\text{TiO}_3\text{--KTaO}_3$  [8];  $\text{Na}_{0.5}\text{Bi}_{0.5}\text{TiO}_3\text{--K}_{0.5}\text{Bi}_{0.5}\text{TiO}_3\text{--K}_{0.5}\text{Na}_{0.5}\text{NbO}_3$  [9];  $\text{K}_{0.5}\text{Bi}_{0.5}\text{TiO}_3\text{--BiScO}_3$  [10];  $\text{BaTiO}_3\text{--Bi}(\text{Mg}_{0.5}\text{Ti}_{0.5})\text{O}_3$  [11–13];  $\text{Bi}_{0.5}\text{Na}_{0.5}\text{TiO}_3\text{--BaTiO}_3$ ,  $\text{CaZrO}_3$  and  $\text{Bi}_{0.5}\text{Na}_{0.5}\text{TiO}_3\text{--BaTiO}_3\text{K}_{0.5}\text{Na}_{0.5}\text{NbO}_3\text{--CaZrO}_3$  [14] and modified  $\text{BaTiO}_3$  [15]. Now-a-days, lots of attention are paid on bismuth based ferroelectrics and related materials, as they are considered as less or non toxic materials (lead-free). Because of having same lone-pair electronic configurations of  $\text{Bi}^{3+}$  and  $\text{Pb}^{2+}$ , possess the same lone-pair electronic configurations, and most of the bismuth based compounds of perovskite family show ferroelectric properties. Since with smaller ionic size,  $\text{Bi}^{3+}$  has been placed at the A-site, not many compounds of bismuth-based perovskite can be prepared by conventional methods at normal pressure. Moreover, complex oxide compositions  $\text{ABO}_3$  (A = mono-divalent, B = tri-to penta-valent ions) favor less close-packed structures. It can be transformed to perovskite structure under high pressure. The high-pressure synthesis and crystal structure solution of meta-stable perovskite  $\text{Bi}(\text{Mg}_{0.5}\text{Ti}_{0.5})\text{O}_3$  (BMT) was reported by Khalyavin et al. [16]. The single-phase ceramics of BMT has not been obtained at normal pressure regardless of what thermal treatment conditions and precursors were used. The perovskite BMT has been synthesized at about 6 GPa and at high temperature. The high-pressure perovskite phase was

✉ Rajib Padhee  
padhee4u@gmail.com

<sup>1</sup> Department of Physics, Siksha ‘O’ Anusandhan University, Khandagiri, Bhubaneswar, Odisha 751030, India

<sup>2</sup> School of Physics, Sambalpur University, Jyoti Vihar, Burla, Sambalpur, Odisha 768019, India

found to be metastable. It was reported that some secondary phases are present in the XRD of resulting ceramic [16]. In view of synthesis of cost effective BMT ceramic, attempt has been made to prepare a single phase material at ambient temperature and pressure. The main objective of the work is to synthesize phase pure at room temperature and characterize it in different experimental conditions to understand the relationship between the structure and properties of a high-temperature perovskite system,  $\text{Bi}(\text{Mg}_{0.5}\text{Ti}_{0.5})\text{O}_3$  (BMT).

## 2 Experimental procedure

The polycrystalline samples of  $\text{Bi}(\text{Mg}_{0.5}\text{Ti}_{0.5})\text{O}_3$  (BMT) were fabricated by a conventional ceramic technique. The starting material for the fabrication of BMT samples are high purity (99%) powder of  $\text{Bi}_2\text{O}_3$  (M/s. CDH),  $\text{TiO}_2$  (M/s. LOBA Chemie Co.) and purity  $\leq 95\%$  of  $\text{MgO}$  (M/s. EMPLURA). The suitable stoichiometric quantity of the constituent materials for the required samples were taken. The powders were dry mixed thoroughly for an hour and wet mixed with methanol by using a mortar and pestle. Mixed powders were kept in an alumina crucible with proper labeling of sample's name and kept in a furnace at temp of  $800\text{ }^\circ\text{C}$  for 4 h. The calcined powder was crushed to make fine powder. The X-ray powder diffraction (XRD) data were collected at room temperature to characterize the crystal structure of the material. The calcined powder was mixed with binder polyvinyl alcohol (PVA). Since PVA is an organic binder, it can be vaporized during high temperature sintering. Then small cylindrical pellets (12 mm diameter) were fabricated from the calcined powder taking the help of a KBr hydraulic press at a pressure of  $5 \times 10^6\text{ Nm}^{-2}$ . After pelletization, the pellets were sintered at  $800\text{ }^\circ\text{C}$  for 4 h. Scanning electron micrograph (SEM) combined with energy dispersive analysis of X-rays (EDAX) and mapping image of elements were recorded of the pellet sample to investigate the microstructure and chemical composition of the pellet sample. Both the parallel surfaces of the a disk shaped pellet was made flat and smooth for electrical measurements. A layer of metallic silver paste with thinner liquid was applied to the sintered pellet followed by heat treatment of  $150\text{ }^\circ\text{C}$  for an hour so as to measure their dielectric and impedance parameters. These electrical parameters (capacitance, dissipation factors, impedance, DC) data were recorded using a computer-interfaced impedance analyzer (phase sensitive meter—PSM 1735, N4L) in a wide range of frequency (1 kHz–1 MHz) at different temperatures (25–480  $^\circ\text{C}$ ). The J–E characteristic of the compound was obtained using a sophisticated electrometer (Keithley, model 6517B).

## 3 Results and discussion

### 3.1 Structural and microstructural studies

Basic crystal data (crystal system unit cell parameter, etc.) of BMT were obtained using powder X-ray diffraction profile (Fig. 1). To obtain these crystal parameters of an unknown system, an attempt was made to index all the peaks of the diffraction profile in seven crystal systems and three different unit cell configurations using a standard computer software 'Powd Mult' [17]. The unit cell dimension of the compound was selected on the basis of best fit (least difference between experimental and theoretical 'd' value of each reflection). As most of the reflections have successfully been indexed, except a few small ones, in a crystal system, we can conclude that the compound has a major orthorhombic phase with a minor unknown impurity phase. Based on the best possible fit and minimum standard deviation (with most of the reflections), the material is considered as an orthorhombic crystal system. The least-squares refined unit cell parameters are:  $a = 25.0237(27)\text{ \AA}$ ,  $b = 8.4153(27)\text{ \AA}$ ,  $c = 8.6711(27)\text{ \AA}$ ,  $V = 1825.97\text{ \AA}^3$  with estimated standard deviation in parenthesis. The normalized unit cell dimension could be written as;  $a' = a/3 = 8.3412\text{ \AA}$ ,  $b' = 8.4153\text{ \AA}$ ,  $c' = 8.6711\text{ \AA}$  which is almost doubling of the distorted perovskite unit cell of such type of material. It clearly supports the reported antiferroelectric phase of the material at room temperature.

The broadness of some peaks suggests that the sample consists of small particles at nano level. The scattered crystallite or particle size (P) of sample is generally estimated using broadening of the profile of the diffraction peak in the

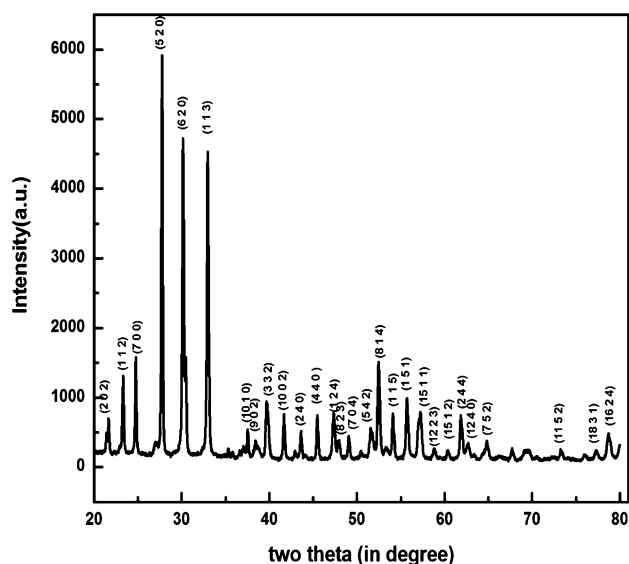


Fig. 1 XRD pattern of  $\text{Bi}(\text{Mg}_{0.5}\text{Ti}_{0.5})\text{O}_3$

Debye–Scherrer’s formula;  $P = \frac{0.89\lambda}{\beta \cos\theta}$  where  $\beta$  = broadening of the diffraction peak measured at half height of maximum intensity (in radian) and  $\lambda = 1.5406 \text{ \AA}$  (wavelength of Cu-K $\alpha$ ) and  $\theta$  is the Bragg’s angle [18]. The average crystallite size of BMT is estimated to be 55 nm. For the calculation of  $P$ , broadening of diffraction peaks also arises due to instrumental effect and lattice strain, which has been ignored since powder sample has been used to record XRD profile.

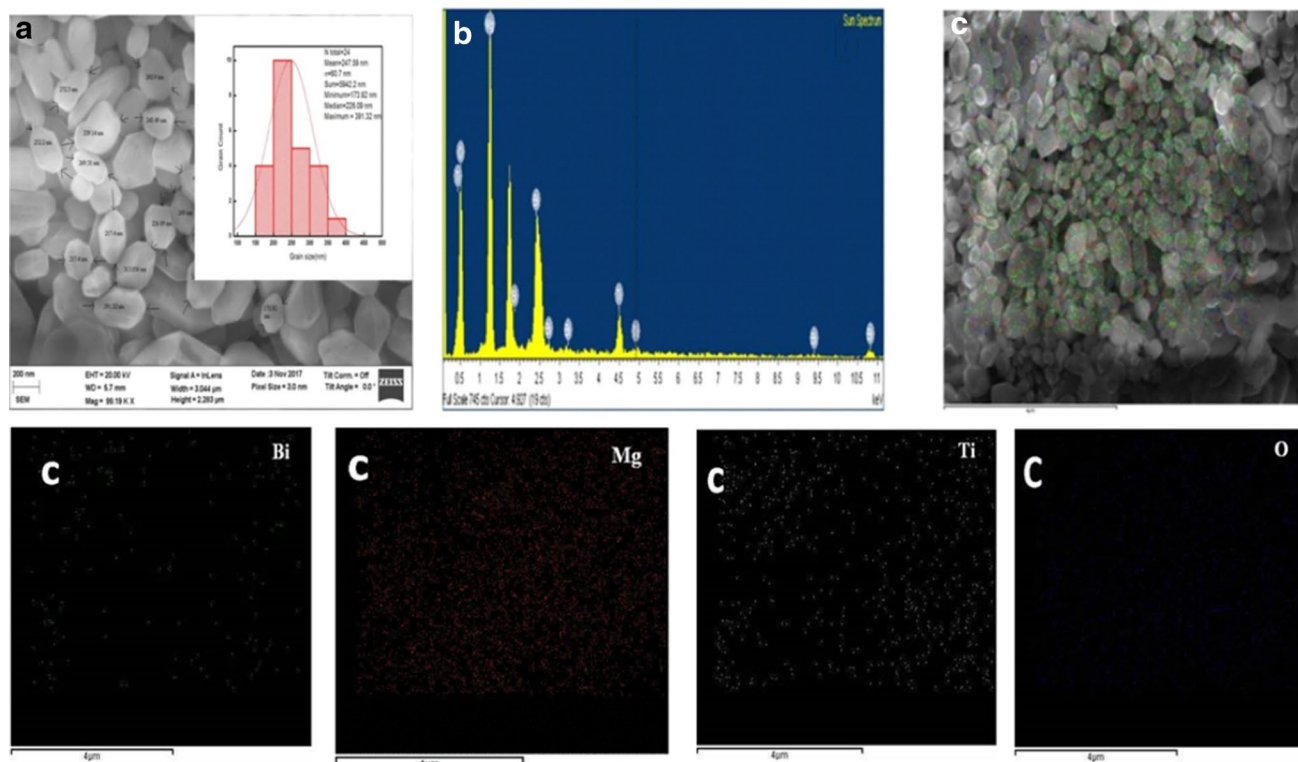
Figure 2a displays the SEM micrograph of the surface of the pellet sample with marked linear dimensions of clear grains. It is observed that grains of different shapes and dimensions are distributed uniformly with a few small voids throughout the surface of the sample. The grain size is found to be in the range of 150–400 nm. The histogram (Fig. 2a(inset)) shows the grain dimension and grain-size distribution on the sample surface. The average grain size calculated from the micrograph is found to be 226 nm.

Figure 2b shows the energy dispersive X-ray (EDX) pattern showing the presence and energy distribution of Bi, Mg, Ti, and O elements. In  $\text{Bi}(\text{Mg}_{0.5}\text{Ti}_{0.5})\text{O}_3$ . Detailed compositional analysis exhibits that the required amount of elements (with small deviation of 2–3%) is present in the prepared compound confirming the stoichiometry of the compound. The wt% of oxygen, magnesium, titanium, bismuth are 39.92, 17.42, 3.96, 25.04 respectively. The at.% of

these element (oxygen, magnesium, titanium, bismuth) has been estimated to be 66.24, 19.03, 2.20, 3.18 respectively. Figure 2c shows the mapping and uniform distribution of content of the sample (Bi, Mg, Ti and O) on the sample surface. The above information confirms the stoichiometry of the prepared sample.

### 3.2 Dielectric study

Figure 3 shows the effect of temperature on (a) permittivity (relative dielectric constant,  $\epsilon_r = Cd/\epsilon_0 A$  where  $C$  = capacitance,  $d$  = thickness,  $A$  = cross-sectional area of the pellet and  $\epsilon_0$  = permittivity of free space) and (b) tangent loss ( $\tan \delta$ ) at some selected frequency. Both the dielectric parameters ( $\epsilon_r$  and  $\tan \delta$ ) decrease on increasing frequency, which is a general feature of dielectric oxide materials. It is illustrated that at low frequency, all the different types of polarizations (interfacial, dipole, atomic, ionic, electronic etc.) exist in the dielectric materials. The existence of these polarizations vanishes slowly on increasing the frequency, as a result, dielectric constant decreases. There are some other reasons (like defects and oxygen vacancies) also for higher value of dielectric constant at low frequency and high temperatures. According to Maxwell–Wagner interfacial polarization model [19], the dispersion or higher value of dielectric constant is observed at low frequency, and is



**Fig. 2** a SEM with grain size distribution, b EDX and c elemental mapping of  $\text{Bi}(\text{Mg}_{0.5}\text{Ti}_{0.5})\text{O}_3$ . (Color figure online)

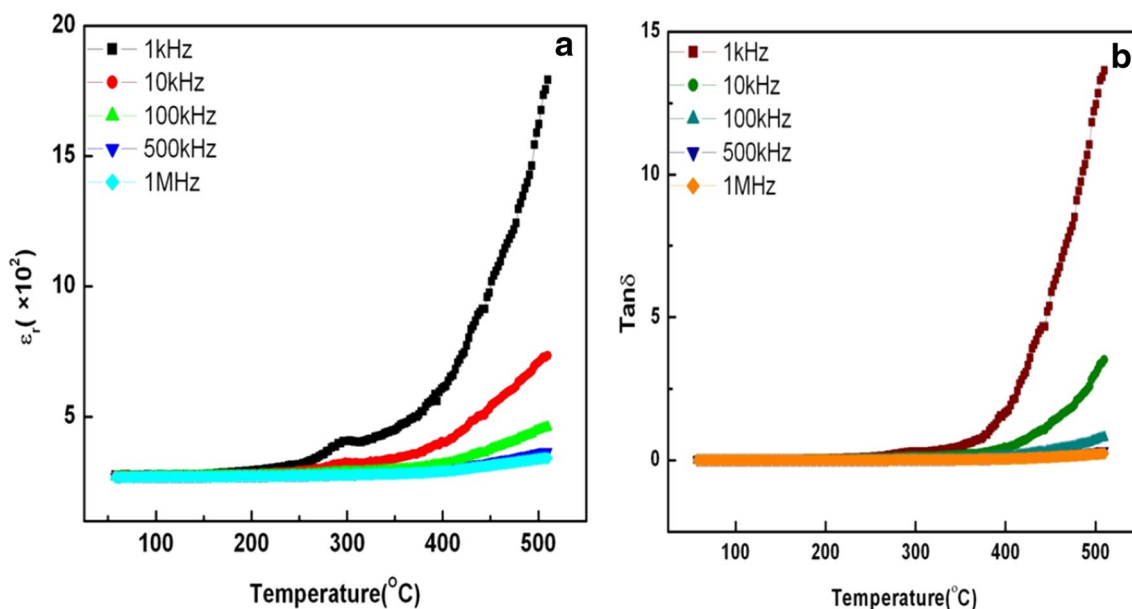


**Fig. 3** Temperature dependence of **a**  $\epsilon_r$  and **b**  $\text{tan } \delta$  of  $\text{Bi}(\text{Mg}_{0.5}\text{Ti}_{0.5})\text{O}_3$  at different frequency. (Color figure online)

in good agreement with Koop's phenomenological theory [20]. As per this model, the dielectric structure of material has two layers: good conducting grains and poorly conducting grain boundaries. In transport process, the electrons are more active at grain boundaries in the low-frequency region, whereas at higher frequency, electrons are more active at grains. In the low-frequency region, for movement of charge carriers more energy is required because of the higher resistance of grain boundaries. So  $\text{tan } \delta$  is high in this region. In the high-frequency region, small energy is needed for the movement of charge carriers because of the low resistance. Thus, the dissipation factor is small in this region. The loss factor is significant for device quality as it describes the energy dissipation in an insulator. A small value of  $\text{tan } \delta$  is needed to ensure low power loss for a good dielectric material. In Fig. 3a, It is noted that the dielectric parameter of the material below 260  $^\circ\text{C}$  is independent of frequency and temperature, suggesting the important role of electronic and/or ionic polarization [21]. With increasing temperature, dielectric permittivity generally increases sharply with a small anomaly or peak. This nature of increase may be explained by scattering of temperature dependent charge carriers or/and defects/impurities present in the sample [22]. The small dielectric anomaly may be related to the suggested antiferroelectric-like phase transition [16] This conclusion can be supported by doubling of the unit cell dimension and occurrence of double hysteresis loop (shown later). Figure 3b exhibits the temperature dependence of  $\text{tan } \delta$  at the selected frequency of the ac electric field. The nature of variation of  $\text{tan } \delta$  as a function of temperature is similar to that of  $\epsilon_r$ . The  $\text{tan } \delta$  increases with rise in temperature and

sharply increases at higher temperatures. This sharp increase is strongly influenced by the electric conductivity [23]. Similar to the dielectric permittivity, an anomaly observed in  $\text{tan } \delta$  near 300  $^\circ\text{C}$ , may also be considered to be related to anti-ferroelectric phase transition which is originated from displacements of  $\text{Bi}^{3+}$  cations and octahedral tilting [16].

### 3.3 Polarisation study

Figure 4 shows the hysteresis loop of BMT at room temperature. The appearance of double hysteresis loop with a small polarization at room temperature confirms the existence of anti ferroelectric nature of the material.

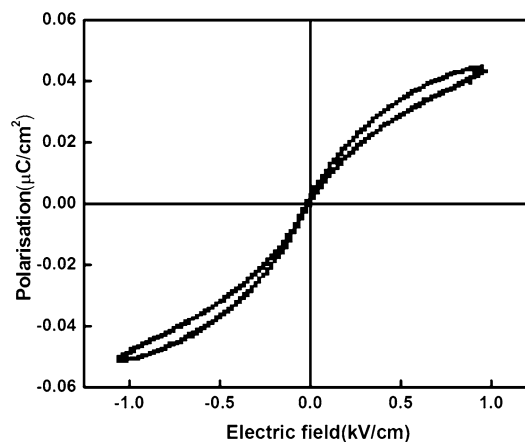


**Fig. 4** Hysteresis loop at room temperature of  $\text{Bi}(\text{Mg}_{0.5}\text{Ti}_{0.5})\text{O}_3$

### 3.4 Impedance study

The electrical properties of the electro-ceramics and ionic conductors (like impedance of grain, grain boundaries and electrodes) can be studied by a nondestructive complex impedance method. It is a powerful tool to provide information about the real part (resistive) and imaginary part (reactive) impedance of a solid sample. The impedance spectroscopy method is mainly used to calculate the impedance and related parameters. In this method, on application of an AC electric field to the sample, field creates a sinusoidal perturbation, and hence impedance and other related parameters are obtained at different frequency and temperatures [24–27].

Figure 5a and b exhibit the frequency variation of  $Z'$  as well as  $Z''$  at different temperatures. The response of applied AC electric field frequency on the sample is commonly understood in terms of complex dielectric constant ( $\epsilon^* = \epsilon' - j\epsilon''$ ), complex impedance ( $Z^* = Z' - jZ''$ ), complex electric modulus ( $M^* = M' - jM''$ ) and dielectric loss, which are related to each other. The following equations describe the real part ( $Z'$ ) and imaginary part ( $Z''$ ) of the complex impedance [28, 29]. Both the above components (real ( $Z'$ ) and imaginary ( $Z''$ )) part of the complex impedance ( $Z^* = Z' - jZ''$ ) can be defined by the following equation [30];

$$Z' = R / \{1 + (\omega\tau)^2\} \text{ and } Z'' = \omega R\tau / \{1 + (\omega\tau)^2\}$$

where  $R$  and  $C$  are the measured resistance and capacitance,  $\omega$  is the angular frequency of the electric field and  $\tau = RC$  is the relaxation time. Relaxation time can be estimated by using the formula  $\tau = R_g C_g$  and taking the value of resistance  $R_g$  and capacitance  $C_g$  of grains/bulk from Table 1. The

**Table 1** Values of  $R_g$ ,  $C_g$  for  $\text{Bi}(\text{Mg}_{0.5}\text{Ti}_{0.5})\text{O}_3$  ceramic at different temperatures

Temperature (°C)	$R_g$ ( $\Omega$ )	$C_g$ (farad)
380	$1.53 \times 10^6$	$1.043 \times 10^{-10}$
400	$5.357 \times 10^5$	$1.052 \times 10^{-10}$
420	$2.257 \times 10^5$	$1.057 \times 10^{-10}$
440	$1.089 \times 10^5$	$1.060 \times 10^{-10}$
460	$6.016 \times 10^4$	$1.049 \times 10^{-10}$
480	$3.503 \times 10^4$	$1.026 \times 10^{-10}$

variation of  $Z'$  with frequency at different temperatures is shown in the Fig. 5a.  $Z'$  decreases with increase in temperature in the region of low frequency indicating the negative temperature coefficient of resistance (NTCR) behavior [31]. It confirms the relaxation properties of sample [32]. The real part of impedance ( $Z'$ ) decreases as frequency and temperature increases pointing an increase in AC conductivity up to a frequency of nearly 50 kHz and after that  $Z'$  values merge into a line suggesting the mechanism of temperature independence and the release of space charge [32]. Similarly, the variation of  $Z''$  with frequency at different temperatures is shown in the Fig. 5b. There is no peak due to the absence of current dissipation of the sample at low temperature. The presence of peak at higher temperature is an indication of the electrical relaxation in the material. The relaxation frequency, at which the imaginary value  $Z''$  reaches a highest limit ( $Z''_{\text{max}}$ ), shift towards the region of higher frequency with increase in temperature. The broadening of peaks and decreasing value of  $Z''_{\text{max}}$  with respect to temperature indicates the occurrence of temperature dependence of relaxation phenomenon of the sample. The relaxation process

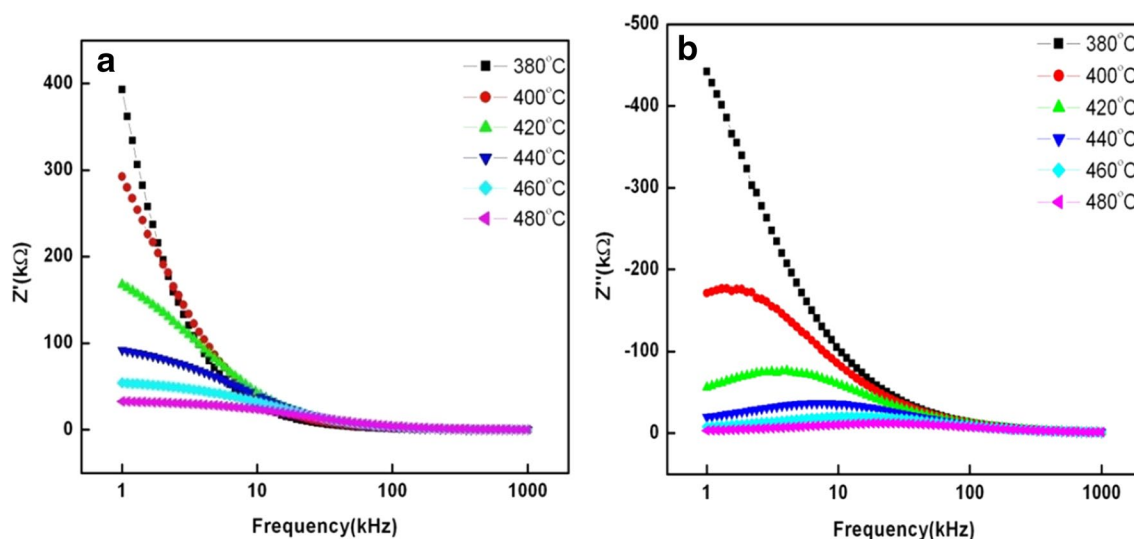


**Fig. 5** Variation of **a**  $Z'$  and **b**  $Z''$  with frequency of applied field at selected temperatures of  $\text{Bi}(\text{Mg}_{0.5}\text{Ti}_{0.5})\text{O}_3$ . (Color figure online)

occurs for deformations and vacancies present in the material at high temperatures [33, 34].

Figure 6 shows the variation of scaling parameters ( $Z''/Z''_{max}$  and  $M''/M''_{max}$ ) with frequency at 440 °C. It can be seen that the peaks are not occurring at the same frequency ( $f_{Z''} < f_{M''}$ ). The magnitude of the mismatch between the peaks of both the parameters represents a change in the apparent polarization. The overlapping of peaks is an evidence of long-range conductivity whereas the difference is an indicative of short-range conductivity (via hopping type of mechanism) [35].

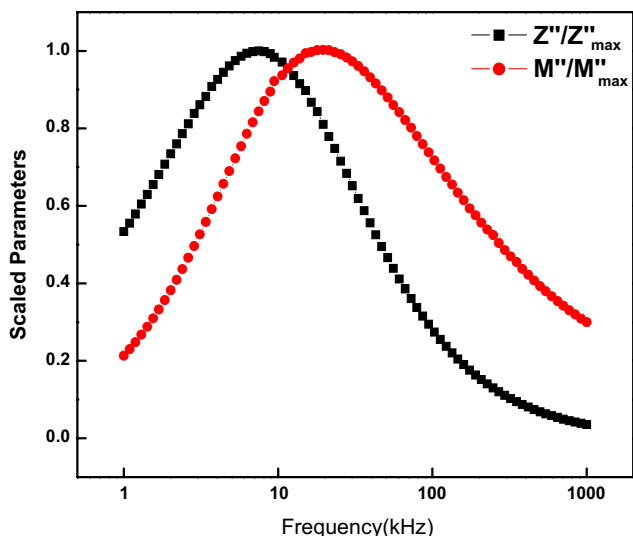


Fig. 6 Variation of normalized  $Z''$  and  $M''$  with frequency for  $\text{Bi}(\text{Mg}_{0.5}\text{Ti}_{0.5})\text{O}_3$  at 440 °C

### 3.4.1 Nyquist diagram

Figure 7a shows the Nyquist diagram (i.e., complex impedance plots ( $Z'$  vs.  $Z''$ )) in the frequency range of (1 kHz–1 MHz) which describes a temperature dependent semicircular arc. When experimental data (real and imaginary component of  $Z$ ) are compared the components of circuit consisting of resistors and capacitors, we get fitting parameters. In this diagram capacitor represents space charge polarization and resistance represents a conductive path. In the figure, the impedance is found to be decreasing along with increasing temperature, thus it depends on the conductivity of the sample. Based on Debye, when we observe a perfect semicircle which centre falls exactly at on the x-axis (real component) we can say, the system has Debye relaxation. But, when the semicircle has its centre below the axis, it is called as non-Debye relaxation process, then we get two circles or semicircles [36, 37]. The intercept of the first semicircle with the  $Z'$  axis provides the grain resistance, and the second semicircle provides grain boundary resistance. A single semicircle is observed in the figure in the high-frequency region at high temperatures. This arc is attributed to conduction of the material due to grain effect. This behavior is due to the contribution of the parallel combination of both the grain capacitance,  $C_g$  and, grain resistance,  $R_g$  (as shown in the inset of Fig. 7) due to the electric relaxation phenomena. Every semicircle at any temperature has its own relaxation frequency, thus the relaxation time ( $\tau$ ) can be estimated using the relation  $\tau = R_g C_g$  where  $x = 2\pi f_{max}$ , and  $f_{max}$  corresponds to the arc maximum where there is no semicircle [38]. In the region of low frequency, which suggests the grain boundaries do not contribute to the impedance or electrical parameters; only

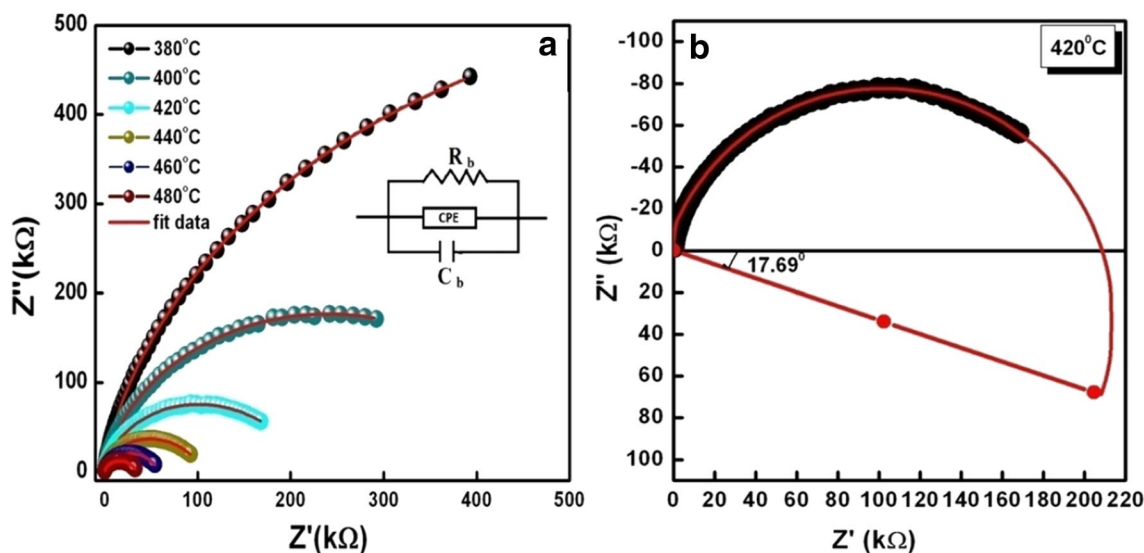


Fig. 7 Variation of  $a Z'$  with  $Z''$  of  $\text{Bi}(\text{Mg}_{0.5}\text{Ti}_{0.5})\text{O}_3$  at different temperatures and  $b$  angle of depression at 420 °C. (Color figure online)

grain conduction occurs in the material. The diameter of the semicircle, as obtained by the intercept of the semicircle with the x-axis, gives the value of  $R_g$ . The experimental values were fitted to an equivalent circuit model using the software ZSimpWin version 2, confirming the accuracy of the experimental data. The non-Debye type behavior was confirmed from the Fig. 7b which shows the depression angle of  $17.6^\circ$  and the centre below the real Z axis at  $420^\circ\text{C}$ . Based on the fitted curve, the values of grain resistance ( $R_g$ ), grain capacitance ( $C_g$ ) at a set of temperature calculated and compared in Table 1.

### 3.5 Electrical conductivity

Figure 8a shows the dependence of AC conductivity ( $\sigma_{ac}$ ) on frequency of the applied electric field and temperatures. Some measured dielectric data have been used to calculate  $\sigma_{ac}$  using the expression;  $\sigma_{ac} = \omega \tan \delta \epsilon_r \epsilon_0$  where  $\omega$  = angular frequency of AC source,  $\tan \delta$  = dielectric loss and  $\epsilon_0$  = dielectric permittivity in vacuum [39].

The variation of  $\sigma_{ac}(\omega)$  with frequency in the range of 1 kHz–1 MHz for the investigated compound was studied through the temperature range of 380–480 °C. The obtained results are plotted as  $\log \sigma_{ac}(\omega)$  versus  $\log \omega$  at different temperature. Figure 8a shows the frequency dependence of AC conductivity of BMT. A linear increase in  $\sigma_{ac}(\omega)$  with an increase of frequency is observed. Initially a plateau region (frequency independent) is observed, which is related to  $\sigma_{dc}$  conductivity. To further increase of the frequency of the applied field, we found increases in conductivity. The nature of the frequency dependent conductivity follows  $\omega^n$  at all the temperatures. The nature of the plots indicates the presence of hopping process in the conduction

process. The hopping frequency increases with rise in temperature. The frequency and temperature dependence of conductivity can be explained using Jonsche's power law [40]:  $\sigma_{ac}(\omega) = \sigma_{dc} + A\omega^n$ , where A is a pre-exponential factor,  $\omega = 2\pi f$  is the angular frequency, n is the power law factor with its value limit  $0 < n < 1$  and other parameters have their usual meaning.

This power law (universal property of materials) can be correlated to the dynamic of hopping conduction process. Some physical process can be related to the value of n. For example, for  $n < 1$ , hopping of the charge carriers is related to the translational motion. But, for  $n > 1$ , a localized small hopping of the charge carriers is considered. This situation and observation clearly suggest an important role of thermal effect in the conduction process. Based on the Jonscher power law, the origin of the AC conductivity and relaxation process and role of conduction electrons in the transport properties of the material can be explained. The low-frequency plateau dispersion region (DC conductivity), associated with AC conductivity, and high frequency dispersion region related to DC conductivity can be understood by power law [19].

Figure 8b shows the variation of AC conductivity ( $\sigma_{ac}$ ) with the inverse of (absolute) temperature K ( $1000/T$ ) at selected frequencies. An increase in the value of  $\log \sigma_{ac}$  when we increase the temperature. This nature of conductivity variation can be understood by considering the movement of charge carriers by hopping, depending on temperature. This situation suggests the semiconductor nature of BMT. The activation energies can be calculated using the Arrhenius Equation:  $\sigma_{dc} = \sigma_0 \exp(-E_a/K_B T)$ , where  $K_B$  = Boltzmann constant,  $\sigma_0$  = pre-exponential factor, and  $E_a$  = activation energy of the charge carriers. Based on the

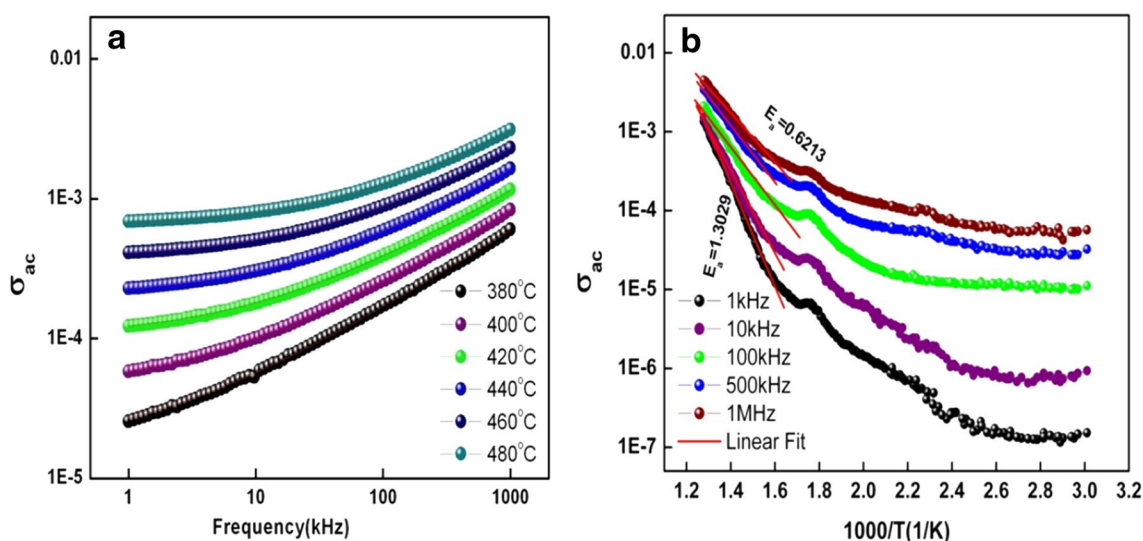


**Fig. 8** a Frequency and b temperature dependence of ac conductivity ( $\sigma_{ac}$ ) of  $\text{Bi}(\text{Mg}_{0.5}\text{Ti}_{0.5})\text{O}_3$ . (Color figure online)

above equation, activation energy of 1.3, 1.03, 0.72, 0.71, 0.62 was found to be at 1, 10, 100, 500 kHz and 1 MHz at high temperatures. The activation energy of the compound decreases with increasing in frequency. It is assumed that activation energy has contributed from the energies required for generation of charge carriers and their motion into the vacancies. For a polycrystalline material, structural defects provide additional acceptor centers at higher temperatures in the polycrystalline sample [40]. As a result, the activation energy is reduced by reducing the participation of acceptor at higher temperatures.

### 3.6 Leakage current characteristics

Figure 9 shows the electric field ( $E$ ) dependence of current density ( $J$ ) of BMT in the temperature range of 50–300 °C on a pellet sample of thickness 0.26 cm and area 1.155 cm<sup>2</sup>. An increase in current density is observed on the increasing electric field at different temperature. A change in the value of leakage current is observed when we increase the temperature. It confirms that the material has thermally assisted conduction process. The current density versus electric field plot is not linear, which confirms that the system exhibit non-Ohmic characteristics.

## 4 Conclusion

Polycrystalline Bi(Mg<sub>0.5</sub>Ti<sub>0.5</sub>)O<sub>3</sub> material was synthesized by a ceramic processing technique (i.e. mixed-oxide route). Preliminary structural analysis using X-ray diffraction data has shown orthorhombic crystal structure of the material. The microstructural analysis with EDX and size histogram of the surface of the pellet sample show almost uniformly

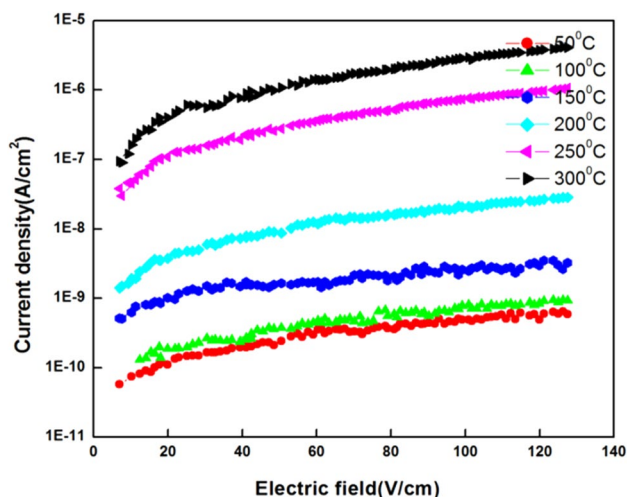


**Fig. 9** Electric field-temperature dependent current density of Bi(Mg<sub>0.5</sub>Ti<sub>0.5</sub>)O<sub>3</sub>

distributed grains of varying shapes and dimensions throughout the surface of the sample. The frequency of the applied AC electric field and temperature strongly affect the dielectric parameters (permittivity and dissipation factor). The presence of a small anomaly in dielectric constant and tangent loss may be related to previously suggested antiferroelectricity in the material. The occurrence of double hysteresis loop (with very small polarization) and doubling of the unit cell dimension of perovskite structure confirms the antiferroelectric nature of the material. The electrical parameters have been obtained from the dielectric and impedance measurements. The high dielectric constant of the material at high temperature has been explained using Maxwell–Wagner model and space charge polarization. Though dissipation factor is temperature dependent, the compound has low tangent loss, even at high temperatures (480 °C at 500 kHz), which decreases as frequency increases. Due to the low tangent loss, the quality factor of the material is high, which is a criterion for many applications including microwave devices. The complex–impedance plots reveal that the material exhibits (i) electrical transport (conduction) due to grains, (ii) negative temperature coefficient of resistance (NTCR) behavior, and (iii) temperature-dependent relaxation phenomenon. The frequency dependence of the AC conductivity obeys Jonscher’s universal power law. The  $J$ – $E$  characteristics indicate a non-Ohmic nature of BMT.

**Acknowledgements** The authors are grateful to, Dr. Satyabati Das (IIT Bhubaneswar) and Madhusmita Sahu (ITER, S’O’A University) for their kind helps in some experiments and analysis work.

## References

1. J.B. Lim, S. Zhang, N. Kim, T.R. Shrout, *J. Am. Ceram. Soc.* **92**, 679 (2009)
2. R. Dittmer, W. Jo, D. Damjanovic, J. Rödel, *J. Appl. Phys.* **109**, 034107 (2011)
3. Y. Saito, H. Takao, T. Tani, T. Nonoyama, K. Takatori, T. Homma, T. Nagaya, M. Nakamura, *Nature* **432**, 84 (2004)
4. N. Raengthon, D.P. Cann, *IEEE Trans. Ultrason. Ferroelectr. Freq. Control* **58**, 1954 (2011)
5. N. Raengthon, T. Sebastian, D. Cumming, I.M. Reaney, D.P. Cann, *J. Am. Ceram. Soc.* **95**, 3554 (2012)
6. T.A. Skidmore, T.P. Comyn, S.J. Milne, *J. Am. Ceram. Soc.* **93**, 624 (2010)
7. F.Y. Zhu, T.A. Skidmore, A.J. Bell, T.P. Comyn, C.W. James, M. Ward, S.J. Milne, *Mater. Chem. Phys.* **129**, 411 (2011)
8. K. Bridger, A.V. Cooke, W.A. Schulze, U.S. Patent No. US 7 697, 263 B2 (2010)
9. R. Dittmer, E.-M. Anton, W. Jo, H. Simons, J.E. Daniels, M. Hoffman, J. Pokorny, I.M. Reaney, J. Rödel, *J. Am. Ceram. Soc.* **95**, 3519 (2012)
10. C. Kruea-In, G. Rujijanagul, F.Y. Zhu, S.J. Milne, *Appl. Phys. Lett.* **100**, 202904 (2012)
11. S. Wada, K. Yamato, P. Pulpan, N. Kumada, B.-Y. Lee, T. Iijima, C. Moriyoshi, Y. Kuroiwa, *J. Appl. Phys.* **108**, 094114 (2010)



12. B. Xiong, H. Hao, S. Zhang, H. Liu, M. Cao, J. Am. Ceram. Soc. **94**, 3412 (2011)
13. Q. Zhang, Z. Li, F. Li, Z. Xu, J. Am. Ceram. Soc. **94**, 4335 (2011)
14. M. Acosta, J. Zang, W. Jo, J. R€odel, J. Eur. Ceram. Soc. **32**, 4327 (2012)
15. B. Tang, S.R. Zhang, X.H. Zhou, Y. Yuan, L.B. Yang, J. Electroceram. **25**, 93 (2010)
16. Khalyavin DD, Salak AN, Vyshatko NP, Lopes AB, Olekhovich NM, Pushkarev AV, Maroz II, Radyush YV, Chem. Mater. **18**, 5104 (2006)
17. E. Wu, *POWDMULT: An Interactive Powder Diffraction Data Interpretation and Indexing Program Version 2.1* (School of Physical Sciences, Flinders University of South Australia, Bradford Park, 2000)
18. G.S. Lotey, N.K. Verma, J. Nanopart. Res. **13**, 5397 (2011)
19. T. Acharya, R.N.P. Choudhary, J. Electron. Mater. **44**, 271 (2015)
20. C.G. Koop, Phys. Rev. **83**, 121 (1951)
21. R.P. Pawar, V. Puri, Ceram. Int. **40**, 10423 (2014)
22. P. Ganguli, S. Devi, A.K. Jha, K.L. Deori, Ferroelectrics **381**, 111 (2009)
23. S. Sahoo, P.K. Mahapatra, R.N.P. Choudhary, M.L. Nandagoswamy, J. Mater. Sci.: Mater. Electron. **26**, 6572 (2015)
24. S. Sen, R.N.P. Choudhary, Mater. Chem. Phys. **87**, 256 (2004)
25. S. Brahma, R.N.P. Choudhary, A.K. Thakur, Phys. B **355**, 188 (2005)
26. J.R. Macdonald, *Impedance Spectroscopy: Emphasizing Solid Materials and Sys-tems.* (Wiley, New York, 1987)
27. J. Suchanicz, Mater. Sci. Eng. B **55**, 114 (1998)
28. A. Rouahi, A. Kahouli, F. Challali, M.P. Besland, C. Vallée, B. Yangui, S. Salimy, A. Goulet, A. Sylvestre, J. Phys. D **46**, 065308 (2013)
29. M. Idrees, M. Nadeem, M.M. Hassan, J. Phys. D **43**, 155401 (2010)
30. M.A. Rahman, A.K.M. Akther Hossain, Phys. Scr. **89**, 115811 (2014)
31. A.R. James, C. Prakash, G. Prasad, J. Phys. D **39**, 1635 (2006)
32. S.C. Panigrahi, P.R. Das, B.N. Parida, R. Padhee, R.N.P. Choudhary, J. Alloy. Compd. **604**, 73 (2014)
33. A.K. Jonscher, Nature **267**, 673 (1977)
34. A. Kumar, B.P. Singh, R.N.P. Choudhary, A.K. Thakur, Mater. Chem. Phys. **99**, 159 (2006)
35. B. Behera, P. Nayak, R.N.P. Choudhary, J. Alloys Compd. **436**, 226 (2007)
36. D.K. Pradhan, R.N.P. Choudhary, C. Rinaldi, R.S. Katiyar, J. Appl. Phys. **106**, 024102 (2009)
37. T. Badapanda, V. Senthil, S.K. Rout, S. Panigrahi, T.P. Sinha, Mater. Chem. Phys. **133**, 863 (2012)
38. B.N. Parida, P.R. Das, R. Padhee, R.N.P. Choudhary, J. Mater. Sci.: Mater. Electron. **24**, 4798 (2013)
39. M. Ram, J. Alloy. Compd. **509**, 1744 (2011)
40. C. Karthik, K.B.R. Varma, J. Phys. Chem. Solids **67**, 2437 (2006)